The Journal of the Acoustical Society of America

JULY 17 2026

Adaptive acoustic beamforming in a turbulent atmosphere

Sergey N. Vecherin ; Michael B. Muhlestein ; Michele L. Eggleston; Matthew J. Kamrath; Vladimir E. Ostashev ; D. Keith Wilson ; Kent L. Gee

Check for updates

J. Acoust. Soc. Am. 160, 629–643 (2026)
https://doi.org/10.1121/10.0044369

View Online
Export Citation

Articles You May Be Interested In

Directional sources and beamforming
Proc. Mtgs. Acoust. (December 2008)

Optimal design of modal beamformers for circular arrays
J. Acoust. Soc. Am. (October 2015)

A time-domain nearfield beamformer with spherical harmonic decomposition
J. Acoust. Soc. Am. (September 2023)

05 August 2026 16:48:48

ASA
LEARN MORE
Advance your science and career as a member of the
Acoustical Society of America

ASA
ACOUSTICAL SOCIETY OF AMERICA

JASA ARTICLE

Adaptive acoustic beamforming in a turbulent atmosphere

Sergey N. Vecherin,[1,a)] Michael B. Muhlestein,[1] Michele L. Eggleston,[1,2] Matthew J. Kamrath,[1] Vladimir E. Ostashev,[1] D. Keith Wilson,[1] and Kent L. Gee[2]

[1]*Cold Regions Research and Engineering Laboratory, U.S. Army Engineer Research and Development Center, 72 Lyme Road, Hanover, New Hampshire 03755, USA*

[2]*Brigham Young University, Provo, Utah 84602, USA*

ABSTRACT:

Acoustic beamforming is widely used for source localization and line-of-bearing determination. Although many different beamforming techniques have been formulated, atmospheric turbulence effects on acoustic arrays are usually ignored in both their theoretical formulation and practical implementation. As a result, the performance of conventional beamformers, formulated for a non-turbulent atmosphere, degrades in the presence of wind velocity and temperature fluctuations, which cause fluctuations in the received signal amplitude and phase. This article presents a mathematical framework in which the amplitude and phase fluctuations are effectively suppressed from the signals allowing application of any beamforming technique and mitigating its performance degradation in a turbulent atmosphere. The framework is constrained to a single source and by the monochromatic plane wave approximation. Application of such an approach to an experiment revealed that the phase and amplitude fluctuations with spatial scales smaller than the array aperture are successfully suppressed, but the larger fluctuations (resulting in wavefront random tilt) remain and cause errors in the line of bearing estimates.

Published 2026. This is a work of the U.S. Government and is not subject to copyright protection in the United States. https://doi.org/10.1121/10.0044369

(Received 14 April 2026; revised 16 June 2026; accepted 18 June 2026; published online 17 July 2026)

[Editor: Karim G. Sabra] Pages: 629–643

05 August 2026 16:48:48

I. INTRODUCTION

Acoustic beamforming (BF) techniques are widely used for source localization and line-of-bearing (LoB) determination. The general idea is to use multiple signal receivers in an array to form a beam as a weighted sum of these signals, which provides a better estimate of the true source signal and its LoB. Each BF technique choses the weights according to a distinct objective function. The simplest one is the delay-and-sum (DaS) beamformer, which synchronizes the signals from all the microphones using time delays and then averages them out. Assuming straight line sound propagation, the time delays are calculated based on the array geometry and the sought direction. This approach yields a better approximation than a single microphone or other non-BF localization techniques because it improves the signal-to-noise ratio for a coherent signal and incoherent noise. Increasing the number of microphones improves the result.

Another widely used technique is minimum variance distortionless response (MVDR) BF, which uses weights that guarantee the minimal variance of the deviation of the estimated signal from the true, but unknown, signal. This approach requires knowledge of the signal-data and data-data covariance matrices, which can be estimated from the measured signals or from theoretical considerations. Moran *et al.* (2007) discusses the details of a practical application of MVDR in moderately complex environmental conditions.

There are many other BF algorithms with various objective functions and degrees of sophistication, such as multiple signal classification (MUSIC) (Licitra *et al.*, 2023), Bayesian (Bell *et al.*, 2000; Yang *et al.*, 2025; Zhang *et al.*, 2025), and maximum likelihood (Collier, 2005; Collier *et al.*, 2005; Meyer *et al.*, 2025). In addition, there are BF formulations accounting for various complications, such as moving sources (Bell and Van Trees, 1998; Moran *et al.*, 2007; Hou *et al.*, 2024), different sensitivity and spatial patterns (Zhao *et al.*, 2024), and uncertainty in data (Song *et al.*, 2009; Itzhak and Cohen, 2024). Although these algorithms can greatly improve array performance when the underlying assumptions regarding the signal and noise structures are met, these beamformers tend to perform unpredictably when these assumptions are not met (Prime and Doolan, 2013; Licitra *et al.*, 2023). One such assumption is that the effect of atmospheric turbulence is negligible. Hereafter, BF techniques formulated for a non-turbulent atmosphere will be called conventional BF techniques.

A wavefront propagating in a turbulent atmosphere can be significantly distorted, resulting in amplitude and phase fluctuations at the aperture of a microphone array (Tatarskii, 1971; Brown and Hall, 1978; Ostashev and Wilson, 2026; Ostashev *et al.*, 2021). Turbulence can lead to intensity fluctuations (scintillations), wander, and spread of an acoustic image. For a 250 Hz source and 770 m path length, Wilson *et al.* (1999) experimentally demonstrated that acoustic images underwent a scintillation of 5.1 dB and a random wander of 1.2° (elevation) and 1.4° (azimuth). A recent

[a)]Email: Sergey.N.Vecherin@usace.army.mil

Published 2026. This is a work of the U.S. Government and is not subject to copyright protection in the United States.

article (Ostashev *et al.*, 2025) provided formulations for the LoB fluctuations in a turbulent atmosphere and showed that the standard deviation (SD) can be on the order of 1° –2° for a propagation distance on the order of hundred meters. Adaptive optics methods have been developed to mitigate turbulence effects in optical images (Lukin, 1996; Andrews and Phillips, 2005; Phillips *et al.*, 2006; Tyson and Frazier, 2022); this continues to be an active area of research. These methods are also used in large arrays of radio telescopes (Intema *et al.*, 2009).

As more formally demonstrated in Sec. II of this paper, the main reason for the performance degradation of the conventional BF techniques in the presence of turbulence is that the BF weights are derived assuming a non-turbulent atmosphere, whereas the measured signals, to which the weights are applied, incorporate turbulence effects (manifested as distortions in their amplitudes and phases). Therefore, to mitigate the degradation and eliminate the mismatch, one of two approaches can be pursued: either to modify the BF mathematical framework to match the signals or to adjust the signals to match the BF framework.

In the former, as an instantaneous state of the random atmosphere is unknown, only statistical inferences can be used, such as the first and second statistical moments, implying ensemble averaging. This approach leads to incorporating models for spatial spectra and covariance (or mutual coherence) functions of turbulent fluctuations. For example, Collier (2005) and Collier *et al.* (2005) estimated the LoB *via* maximum likelihood assuming the von Karman spatial spectrum for turbulence, theoretical mutual coherence functions for signal fluctuations (both transversal and longitudinal), the statistical independency of the signal measurements in time, and a near-normal incidence direction. Although such an approach represents a systematic way to incorporate signal propagation effects in the turbulent atmosphere for LoB estimates, it has some limitations and inconveniences for practical applications. First, it does not improve the signal-to-noise ratio because there is no summation of the signals measured at the microphones at the same time. Second, it is not compatible with conventional BF formulations. Third, it does not eliminate instantaneous signal distortions.

Therefore, this paper explores the second approach, which (partially) eliminates the measured signal distortions at any particular time of LoB estimation (i.e., without ensemble averaging). After such filtration, any conventional BF technique can be applied to the adjusted signals. In this approach, all the benefits of conventional beamformers are preserved, such as increasing the signal-to-noise ratio, maintaining numerical efficiency (only linear algebra is used), and preserving the desired optimality when computing the weights. The developed framework is demonstrated using experimental data recorded by an acoustic camera for a monochromatic single source in a turbulent atmosphere. The results indicate that the proposed technique significantly improves BF performance in a turbulent atmosphere with respect to some metrics defined in Sec. III. However, the signal amplitude and phase fluctuations at the spatial scales larger than the array aperture cannot be filtered out by this technique and, therefore, still cause errors in the LoB estimates.

II. METHOD

A. BF in the absence of turbulence

The BF mathematical model adopted in this paper is based on the work of Bell *et al.* (2002), which was formulated for the homogeneous atmosphere without turbulence as

$$x_m(t) = \sum_{d=1}^{D} A_{md} s_d(t) + n_m(t), \tag{1}$$

where all signals and noise are zero-mean and complex-valued, $x_m(t)$ is a signal measured at the mth microphone in an acoustic array at time t, $m = 0, \ldots, M-1$, d is a subscript corresponding to different directions of signal arrival, A_{md} is the phasor for microphone m in the direction d, $s_d(t)$ is an incident signal from the direction d, and $n_m(t)$ is the noise at the location of the mth sensor. Note that the noise $n_m(t)$ does not represent the noise because of a turbulent atmosphere. The latter causes the propagation speed to be random, which translates to the randomization of the signal amplitude and phase and, eventually, results in a multiplicative noise factor in phasors A_{md} that cannot be incorporated into the additive noise $n_m(t)$. Equation (1) assumes a non-turbulent atmosphere.

In practice, the complex-valued signals are obtained from real-valued measurements by using Fourier or Hilbert transforms. In this article, a short-term (1 s time series) Fourier transform was used to obtain the complex signals at the frequencies of interest. The noise at the sensors is assumed to be uncorrelated with any signal and between any pair of sensors indexed by m and l,

$$\langle n_m \rangle = 0, \quad \langle n_m s_d^* \rangle = 0, \quad \langle n_l n_m^* \rangle = \sigma_m^2 \delta_{ml}, \tag{2}$$

where σ_m^2 represents the noise power at the mth sensor, $*$ stands for complex conjugate, δ_{ml} is the Kronecker delta, and the angular brackets denote an ensemble average. The physical meaning of the model in Eq. (1) is that the signal at each microphone is the sum of all the signals incident on that sensor from all directions plus a noise at the microphone location. In this article, consideration is limited to a monochromatic acoustic point source located far enough from the acoustic array so that the plane wave approximation is applicable.

For a single frequency f and a plane wave arriving from direction d, the phasors are given by

$$A_{md} = e^{i\Phi_{md}}, \tag{3}$$

where $\Phi_{md} = \mathbf{k}_d \cdot \mathbf{r}_m$ is the plane wave phase for microphone m from the direction d relative the coordinate system origin ($\mathbf{r} = 0$), $\mathbf{k}_d$ is the incident wave vector,

05 August 2026 16:48:48

https://doi.org/10.1121/10.0044369

$k = |\boldsymbol{k_d}| = 2\pi f/c$, where c is the adiabatic sound speed, and vector $\mathbf{r}_m$ characterizes the location of the mth microphone. The phases can be calculated from the array geometry. For a linear array with equally spaced microphones, as depicted in Fig. 1(a), the phases are given by

$$\Phi_{md} = km\Delta r \cos\varphi_{d,} \tag{4}$$

where Δr is the distance between adjacent microphones, and the angle φ_d characterizes the direction of the incident wave. For a two-dimensional (2D) planar array with the circular geometry shown in Fig. 1(b), which will be used in this paper, the relative phases can be expressed in the spherical coordinate system, in which the y and z axes form an array plane, and the x axis is defined by the right-hand rule,

$$\begin{aligned}
&\mathbf{k}_d = (k\sin\theta_d\cos\varphi_d,\ k\sin\theta_d\sin\varphi_d,\ k\cos\theta_d),\\
&\mathbf{r}_m = (0,\ r_m\sin\theta_m \mathrm{sgny}_m\,,\ r_m\cos\theta_m),\\
&\Phi_{md} = kr_m(\sin\theta_d\sin\varphi_d\sin\theta_m \mathrm{sgny}_m + \cos\theta_d\cos\theta_m),
\end{aligned} \tag{5}$$

where the microphone locations $\mathbf{r}_m$ are determined by the radius and the polar angle, $(r_m,\ \theta_m)$, in the array plane (with the azimuthal angle $\varphi_m = 90^\circ sgny_m$ for any m), as shown in the middle expression in Eq. (5), and the incident direction is characterized by the plane wave vector $\mathbf{k}_d$ with the polar and azimuthal angles $(\theta_d,\ \varphi_d)$: $\theta_d \in [0^\circ,\ 180^\circ]$, $\varphi_d \in [-180^\circ,\ 180^\circ]$.

The objective of BF is to numerically construct a beam $b(t)$ in a certain direction d as a linear combination of measured signals on each microphone,

$$\mathbf{B} = \mathbf{W}^{\mathrm{H}}\mathbf{X}, \tag{6}$$

where the superscript H indicates a conjugate transpose, $\mathbf{B}$ represents the beams formed in all incident directions (t varies along columns, the direction index d varies along the rows), and $\mathbf{X}$ is a matrix of signals recorded at all sensors (t varies along columns, the sensor index m varies along the rows),

$$\mathbf{X} = [x_0(t), \ldots, x_{M-1}(t)]^{\mathrm{T}}, \tag{7}$$

the superscript T stands for a matrix transpose, and the weights $\mathbf{W}$ are determined for each direction in accordance with various objective functions. For a monochromatic plane wave, DaS BF takes a particularly simple form, because the time delays (DaS is typically formulated in the time domain) are equivalent to phase shifts for a plane wave, which is represented by the phasors

$$\mathbf{W}^{\mathrm{H}} = \frac{1}{M}\mathbf{A}^{\mathrm{H}}. \tag{8}$$

This equation has a clear physical interpretation: the beam consists of the algebraic average of all signals recorded on the microphones, with phase delays appropriate to bring them in phase given the direction of the incident wave.

The optimal weights for MVDR BF are quite different and depend on the correlation properties of the measured data and the true signal (e. g., Bell *et al.*, 2002),

$$\mathbf{W}^{\mathrm{H}} = \mathbf{R}_{sx}\mathbf{R}_{xx}^{-1}, \tag{9}$$

where $\boldsymbol{R}_{sx}$ and $\boldsymbol{R}_{xx}$ are cross- and auto-covariance matrices between the sought and measured signals, and the superscript -1 stands for a matrix inverse. Using the definition of cross- and auto-covariance and the underlying model of Eq. (1), one can obtain analytical expressions for $\boldsymbol{R}_{sx}$ and $\boldsymbol{R}_{xx}$ as

$$\mathbf{R}_{xx} = \langle x_m(t)x_n^*(t)\rangle = \mathbf{A}\mathbf{R}_{ss}\mathbf{A}^{\mathrm{H}} + \boldsymbol{\sigma}^2, \tag{10}$$

where $\boldsymbol{\sigma}^2 = \mathrm{diag}(\sigma_m^2)$ is the diagonal matrix of noise variances on all microphones, $\boldsymbol{R}_{ss} = \langle s_{d_1}(t)s_{d_2}^*(t)\rangle$ is the covariance matrix of signals incident from different directions, and

$$\mathbf{R}_{sx} = \langle s_d(t)x_n^*(t)\rangle = \mathbf{R}_{ss}\mathbf{A}^{\mathrm{H}}. \tag{11}$$

If the signals incident from different directions are uncorrelated (which is not always the case) or for the case of a single source, which is considered in this paper,

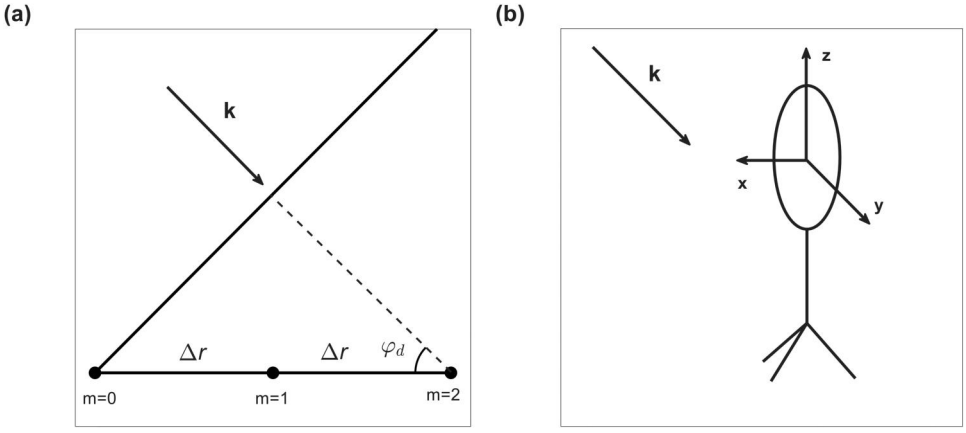


FIG. 1. Array geometries and the direction of incident wave. (a) Linear one-dimensional array, (b) planar two-dimensional array (acoustic camera).

05 August 2026 16:48:48

$$\mathbf{R}_{ss} = \mathbf{P}, \tag{12}$$

where $\mathbf{P} = \mathrm{diag}(P_d)$ is the diagonal matrix of signal powers in distinct directions. For a single source, only a single element in $\mathbf{P}$ is non-zero. The theoretical covariance matrices are seen to be defined solely through the steering matrix $\mathbf{A}$, which reflects the geometry of the array and assumes undistorted phase incident from a specific direction.

Figure 2 shows the 384-microphone array of the acoustic camera used in the experiment and the corresponding magnitude and phase of the theoretical $\boldsymbol{R}_{xx}$ matrix calculated using Eq. (10) for a unit power, monochromatic ($f = 450\,\mathrm{Hz}$) plane wave incident from the direction $\theta_d = 135^\circ$, $\varphi_d = 45^\circ$. The array consists of three identical panels with 128 microphones each. The signal-to-noise power ratio is set to 0.1.

As seen in Fig. 2(b), the magnitude of $\boldsymbol{R}_{xx}$ is constant and equal to the power of the incident signal, except for the main diagonal, where the signal power is increased by the additive (statistically independent) noise power. The phase of $\boldsymbol{R}_{xx}$ represents phase differences between each pair of microphones in the array and, therefore, is defined by the array geometry and the incident wave direction. In general, the magnitude matrix is symmetric, and the phase matrix is antisymmetric relative to the main diagonal. The abrupt phase changes in Fig. 2(c) are because of phase wrapping to $[-\pi, \pi]$ interval.

Equations (10)–(12) allow for analytical calculations of the cross- and auto-covariance matrices if the geometry of the array, noise power, and incident signal power and direction are known; i.e., they solve the forward problem. In practice, for a signal detection, the signal powers and incident directions are unknown. In other words, the inverse problem should be solved, when the geometry of the array and the measured signal covariance matrix are known, but the power and direction of the incident wave are subject to determination. They can be estimated from the measured signals using the Capon formula (e.g., Stoica *et al.*, 2002),

$$\widehat{P}_d = \frac{1}{\mathbf{A}_d^{\mathrm{H}} \widehat{\mathbf{R}}_{xx}^{-1} \mathbf{A}_d}, \tag{13}$$

where $\widehat{P}_d$ is the estimated signal power in the direction d, $\boldsymbol{A}_d$ is the dth column-vector of matrix $\mathbf{A}$, and $\widehat{\boldsymbol{R}}_{xx}$ is the empirical signal covariance matrix, estimated from the measured signals using time-averaging,

$$\widehat{\mathbf{R}}_{xx} = \frac{1}{N} \mathbf{X}\mathbf{X}^{\mathrm{H}}, \tag{14}$$

where N is the number of samples in the measured signal $x(t)$. The time interval for averaging might be large if the sought signals and noise are statistically stationary. Alternatively, the time window could be short (but still long enough for meaningful statistical averaging), and $\widehat{\boldsymbol{R}}_{xx}$ can be re-calculated every time the estimation of the LoB or source location is needed. These empirically estimated $\widehat{\boldsymbol{R}}_{xx}$ and $\widehat{P}_d$ are used in Eq. (9) to calculate the optimal weights for MVDR BF. It is worth noting that the MVDR weights satisfy the constraint of a distortionless response,

$$\mathbf{W}^{\mathrm{H}} \mathbf{A} = \mathbf{I}, \tag{15}$$

where $\mathbf{I}$ is the identity matrix.

Once the weights are calculated, the beam power in any direction can be found through the measured signals using Eq. (6),

$$\mathbf{P}_b = \mathrm{diag}\left(\langle \mathbf{B}\mathbf{B}^{\mathrm{H}} \rangle_t\right) = \mathrm{diag}\left(\mathbf{W}^{\mathrm{H}} \widehat{\mathbf{R}}_{xx} \mathbf{W}\right). \tag{16}$$

The highest beam power location in the (θ_d, φ_d) plane indicates the incident direction.

B. BF in turbulence

As can be seen from Eqs. (8)–(11), the beamformer's weights are determined by the steering matrix $\mathbf{A}$ and the signal covariance matrices, which are also dependent on $\mathbf{A}$. This steering matrix is calculated by Eqs. (3) and (5), which assume a non-turbulent atmosphere. However, turbulence leads to amplitude and phase distortions of the incident plane wave. Therefore, when forming a beam with Eq. (6) using experimentally measured signals $\mathbf{X}$, there is no correspondence between the weights calculated assuming a non-

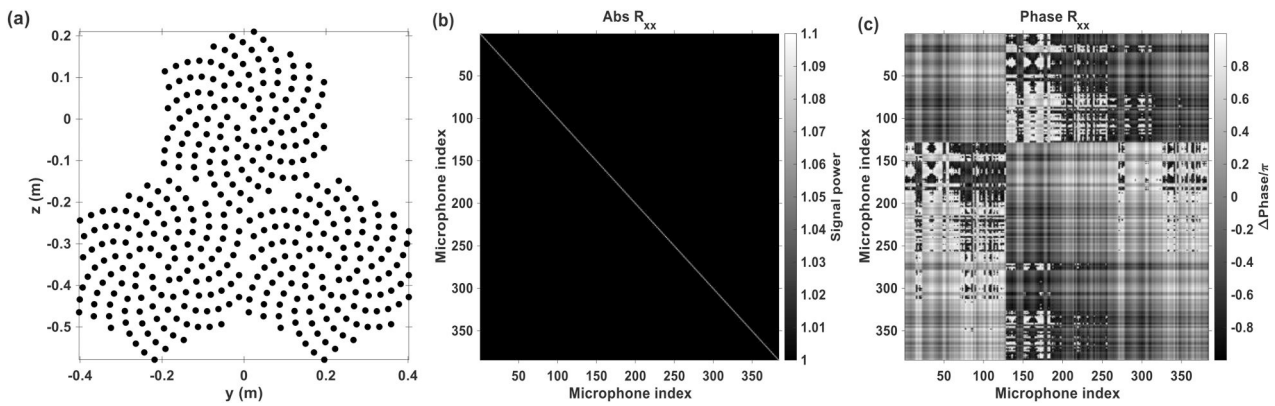


FIG. 2. Acoustic camera and analytical covariance matrix $\boldsymbol{R}_{xx}$ for $f = 450\,\mathrm{Hz}$. (a) Microphone array geometry of the acoustic camera used in the experiment, (b) magnitude (Abs) of analytical $\boldsymbol{R}_{xx}$, (c) phase of analytical $\boldsymbol{R}_{xx}$.

05 August 2026 16:48:48

https://doi.org/10.1121/10.0044369

turbulent atmosphere and the experimental signals that necessarily include all the effects of turbulence. As a result, the beam energy footprint might become blurred and asymmetric (Dougherty, 2002), which causes larger LoB errors and degraded overall performance. The objective of the method described below is to preprocess the empirical signals so that conventional beamformers maintain their performance even in a turbulent atmosphere.

The empirical phase of the signal on microphone m coming from direction d and propagating in the turbulent atmosphere, $\tilde{\Phi}_{md}$, can be represented as

$$\tilde{\Phi}_{md} = \hat{\Phi}_{md} + \varepsilon_{md}, \tag{17}$$

where $\hat{\Phi}_{md}$ is the plane wave phase, and ε_{md} is a non-plane wave phase distortion that might be caused by variety of phenomena, such as noise, a non-plane wave source, interaction with reflected and scattered waves, and turbulence. In the ideal case, if there were no other plane wave phase contributions from clutter, $\hat{\Phi}_{md}$ would be equal to the analytical value of Φ_{md} given by Eq. (5). Given $\tilde{\Phi}_{md}$, our objective is to separate $\hat{\Phi}_{md}$ from ε_{md} and then use the resulting value of $\hat{\Phi}_{md}$ in the BF framework, in lieu of Φ_{md}. This separation can be achieved using the Zernike polynomials, which are a sequence of 2D functions that are orthogonal on the unit disk and are often used in image processing and analysis (Andrews and Phillips, 2005; Phillips *et al.*, 2006; Tyson and Frazier, 2022). Although there are other orthogonal polynomials that can be used for a 2D function decomposition, Zernike polynomials are specifically designed for 2D circular arrays and have a clear interpretation of their terms. Notably, the first three terms are sufficient to represent the spatial distribution of a plane wave's phase on the array aperture. The higher order polynomials describe the deviations of the wavefront from its plane wave approximation. The measured phase $\tilde{\Phi}_{md}$ at a microphone with coordinates (r_m, θ_m) can be decomposed into the following series:

$$\tilde{\Phi}_{md}\left(\frac{2r_m}{D}, \tilde{\theta}_m\right) = \sum_{i=1}^{\infty} a_i Z_i\left(\frac{2r_m}{D}, \tilde{\theta}_m\right), \tag{18}$$

where a_i are direction-specific constant coefficients (d is a silent index), D is the diameter of the circular planar array, $\tilde{\theta}_m \in (-\pi, \pi]$ is the azimuthal angle of the mth microphone in the yz-plane of the array, $\tilde{\theta}_m = arctanz_m/y_m$, ($\pm\pi$, if necessary, to maintain a correct quadrant), and Z_i are the Zernike polynomials indexed by a sequential single index instead of the conventional two indices using Noll's convention (On-Line Encyclopedia of Integer Sequences (OEIS), 2026). The first six Zernike polynomials are presented in Table I.

The most important property of the Zernike polynomials for the present approach is that the first three functions correspond to the plane wave piston and tilt along the cardinal axes of the array plane. Therefore, for a plane wave incident from any direction, only three terms are needed to describe its phase distribution on the array, whereas higher indexed functions describe non-plane wave contributions. Figure 3 verifies this statement showing the maximum absolute error (among all possible incident directions) in the decomposition of the analytical plane wave phases given by Eq. (5) as the function of the number of terms used in the decomposition. As seen in Fig. 3, regardless of the incident direction, the plane wave phases require only three terms in the decomposition; the maximum absolute error between the original and decomposed phases drops to and remains at zero starting with index 3. In practical applications, caution should be taken when the measured phases are used for the decomposition because Eq. (5) represents unwrapped phases. Therefore, the experimentally measured phases should be spatially unwrapped before using the decomposition.

TABLE I. First six Zernike polynomials, sequentially indexed.

$Z_1(r,\theta) = 1$	$Z_4(r,\theta) = \sqrt{3}(2r^2 - 1)$
$Z_2(r,\theta) = 2r\cos\theta$	$Z_5(r,\theta) = \sqrt{6}r^2\sin(2\theta)$
$Z_3(r,\theta) = 2r\sin\theta$	$Z_6(r,\theta) = \sqrt{6}r^2\cos(2\theta)$

The consequence of such a property is that the first three coefficients of the decomposition appear only in the first term in Eq. (16). Using the property of polynomials orthogonality, these three coefficients could have been estimated directly by integration of $\tilde{\Phi}_{md}$. However, such a procedure requires that $\tilde{\Phi}_{md}$ is known on the array plane with arbitrary precision (or at least with high resolution on the plane) to allow numerical integration with the required accuracy. This requirement is challenging in practice because the phase can only be measured at the microphone locations, which are not uniformly distributed on the plane, e.g., see Fig. 2(a). Therefore, a more robust procedure is to use least-square estimation for these three coefficients,

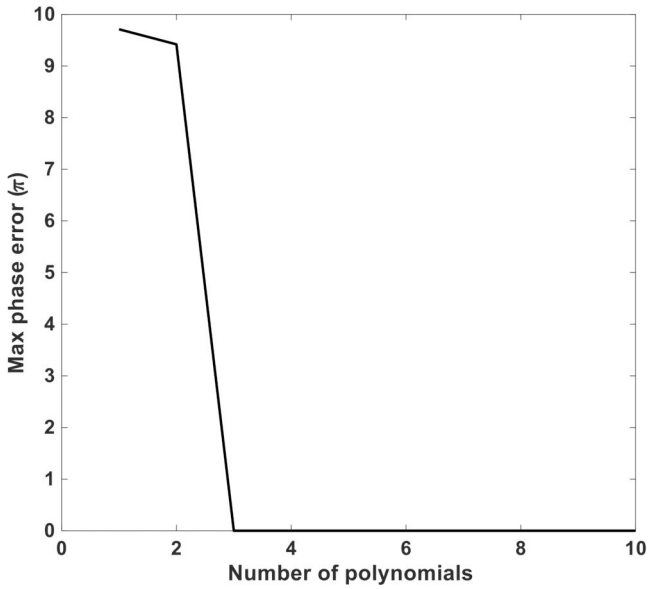


FIG. 3. For all incident plane wave directions, the maximum absolute phase decomposition error vs the number of polynomials used in the decomposition. Max, maximum.

05 August 2026 16:48:48

$$\mathbf{a} = (\mathbf{Z}^{\mathrm{T}}\mathbf{Z})^{-1}\mathbf{Z}^{\mathrm{T}}\tilde{\mathbf{\Phi}}, \tag{19}$$

where $\mathbf{a} = [a_1, a_2, a_3]^{\mathrm{T}}$ is the column-vector of the decomposition coefficients,

$$\mathbf{Z} = \begin{bmatrix} Z_1\left(\frac{2r_1}{D}, \tilde{\theta}_1\right) & Z_2\left(\frac{2r_1}{D}, \tilde{\theta}_1\right) & Z_3\left(\frac{2r_1}{D}, \tilde{\theta}_1\right) \\ \vdots & \vdots & \vdots \\ Z_1\left(\frac{2r_M}{D}, \tilde{\theta}_M\right) & Z_2\left(\frac{2r_M}{D}, \tilde{\theta}_M\right) & Z_3\left(\frac{2r_M}{D}, \tilde{\theta}_M\right) \end{bmatrix}, \tag{20}$$

and

$$\tilde{\mathbf{\Phi}} = \left[\tilde{\Phi}\left(\frac{2r_1}{D}, \tilde{\theta}_1\right), \ldots, \tilde{\Phi}\left(\frac{2r_M}{D}, \tilde{\theta}_M\right)\right]^{\mathrm{T}}, \tag{21}$$

is the column-vector of the measured phases on all the microphones. Note that for three or more microphones, $M \geq 3$, the matrix $\boldsymbol{Z}^T\mathbf{Z}$ is well-conditioned and invertible. Once the coefficients are estimated, the desired plane wave phases on the microphones are found as $\hat{\mathbf{\Phi}} = \mathbf{Za}$.

For convenience, BF results are usually expressed not in terms of the incident plane wave direction characterized by (θ_d, φ_d) but by the LoB direction (pointing to the source location) characterized by angles $(\theta_{LoB}, \varphi_{LoB})$,

$$\theta_{\mathrm{LoB}} = 180^\circ - \theta_d, \quad \varphi_{\mathrm{LoB}} = \begin{cases} \varphi_d + 180^\circ, & \varphi_d \leq 0 \\ \varphi_d - 180^\circ, & \varphi_d > 0. \end{cases} \tag{22}$$

For a measured signal, the amplitude of the incident wave also undergoes distortions because of scattering, ambient and instrumental noise, and turbulence. In fact, while validating the experimental data, it was revealed that the instrumental noise was significant. Specifically, many microphones showed substantial differences in the amplitude of the same signal, and one panel in the acoustic camera had a large phase delay compared to the other two. Both facts indicate substantial instrumental errors in data acquisition. As the result, an example short-term (1 s time series) empirical covariance matrix (Fig. 4) looks completely different from its theoretical counterpart, Figs. 2(b) and 2(c).

The magnitude of the first panel [the upper left square of 128×128 microphones in Fig. 4(a)] is consistently larger than at the other two panels, and the phase on the second panel [the middle square of 128×128 microphones in Fig. 4(b)] is excessively corrupted within itself and consistently different from the other two panels. Although distortions are expected in the empirical signals, they would be similar on all microphones if the cause is just environmental noise and turbulence. Therefore, in this experiment, the instrumental noise played a major role. Note that the proposed technique for suppressing signal amplitude and phase fluctuations because of turbulence also filters out this instrumental noise.

The next step is to filter out these effects in the plane wave empirical covariance matrix. The empirical covariance matrix of the microphone signals propagated in the turbulent atmosphere $\tilde{\boldsymbol{R}}_{xx}$. can be presented similarly to Eq. (16) as the sum of the plane wave covariance matrix $\hat{\boldsymbol{R}}_{xx}$ and a matrix containing all other non-plane wave contributions. Similarly to the phase adjustments, the idea here is to estimate the plane wave matrix $\hat{\boldsymbol{R}}_{xx}$ given its non-plane wave empirical counterpart $\tilde{\boldsymbol{R}}_{xx}$. In the ideal case (no turbulence, a single monochromatic source, and the plane wave approximation holds true), the structure of the analytical covariance matrix $\boldsymbol{R}_{xx}$ is known [see Figs. 2(b) and 2(c)]. In the empirical matrix $\tilde{\boldsymbol{R}}_{xx}$, the phases are antisymmetric by construction (which is a physically correct outcome), but the magnitudes might be corrupted. Therefore, to filter out all non-plane wave effects on the magnitude, the empirical matrix magnitudes can be adjusted as follows: all the diagonal elements are set to the mean of all the diagonal elements, and all the other elements are set to the mean of all the non-diagonal elements. This procedure results in the plane wave matrix $\hat{\boldsymbol{R}}_{xx}$. The amplitude of the incident plane wave is then estimated as the square root of a non-diagonal element. Knowing the amplitude and phases of $\hat{\boldsymbol{R}}_{xx}$, one can adjust

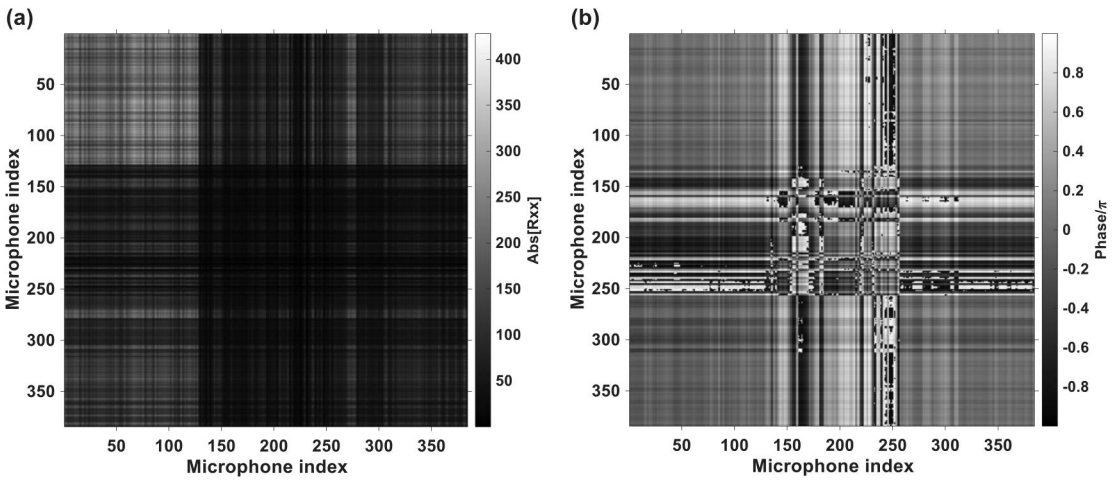


FIG. 4. Empirical covariance matrix $\hat{\boldsymbol{R}}_{xx}$ at $f = 450$ Hz (compare with Fig. 2). (a) Magnitude (Abs), (b) phase.

05 August 2026 16:48:48

https://doi.org/10.1121/10.0044369

the measured signals $\mathbf{X}$ to make them compatible with the assumption of a single incident plane wave.

Making these adjustments to the signals and their covariance matrices and using these quantities in the BF formalism together eliminates small-scale turbulence effects. If turbulence (or anything else) causes a spurious wavefront tilt across the entire array, these effects will not be reduced but instead will be counted as legitimate plane wave contributions. For this reason, the proposed technique does not eliminate errors in the LoB because of sound refraction.

This limitation of the proposed algorithm can be understood in terms of the coherence radius, which plays a key role in sound propagation in a turbulent atmosphere (Ostashev and Wilson, 2026). The phase correction, as described by Eq. (17), depends on whether the array aperture, D, is smaller or larger than the coherence radius r_{coh} of a sound wave in a turbulent atmosphere. The coherence radius is the distance along the wavefront at which the sound field remains about the same. In a turbulent atmosphere, the wavefront is split into many areas of size r_{coh}, which can be considered as locally plane and propagating in different directions (manifesting random refractions). If $D \lesssim r_{coh}$, the wavefront at the array aperture is approximately plane. The suggested approach determines the wavefront tilt (*via* $\widehat{\Phi}_{md}$) and removes the small deviations ε_{md} from the phases corresponding to the plane wave approximation. The wavefront tilt is a sum of the true tilt (corresponding to the source direction) and its fluctuation because of refraction caused by turbulence. The latter is not removed in a short-term measurement but can be removed when time averaging is applied (e.g., long-term MVDR), as described below. On the other hand, if $D \gg r_{coh}$, the wavefront on the aperture is split into many locally plane areas with different tilts and propagation directions. In this case, the random tilts from different areas average to zero when the proposed technique is applied so that the estimated phase corresponds to the true tilt, $\widehat{\Phi}_{md} \cong \Phi_{md}$.

The estimate of the coherence radius for this experiment is the following. Ostashev *et al.* (2025) provides the theoretical variance of the LoB fluctuations as measured with the two-element interfereometer,

$$\sigma_\theta^2 = \frac{D_\phi(r)}{k^2 r^2}. \tag{23}$$

Here, r is the distance between two microphones, and $D_\phi(r)$ is the structure function of the phase fluctuations ϕ [the fluctuating part of $\widehat{\Phi}_{md}$ in Eq. (5) relative to its mean value]. The mutual coherence function of the sound field, $\Gamma(r)$, can also be expressed in term of $D_\phi(r)$, e. g., Rytov *et al.* (1989) and Ostashev *et al.* (2024),

$$\Gamma(r) = |p_0(r)|^2 \exp\left(\frac{-D_\phi(r)}{2}\right), \tag{24}$$

where $p_0(r)$ is the sound field in free space. For the Kolmogorov spectrum of turbulence, using Eqs. (7.208) and (7.209) in Ostashev and Wilson (2026), the mutual coherence function can be written as

$$\Gamma(r) = |p_0(r)|^2 \exp\left[-\left(\frac{r}{r_{coh}}\right)^{5/3}\right]. \tag{25}$$

From Eqs. (24) and (25), one has $D_\phi(r) = 2(r/r_{coh})^{5/3}$. Substituting this formula into Eq. (23) and solving the resulting equation for r_{coh} yields

$$r_{coh} = \frac{2^{3/5}}{k^{6/5} r^{1/5} \sigma_\theta^{6/5}}. \tag{26}$$

Here, $\sigma_\theta = \sqrt{\sigma_\theta^2}$ is the LoB SD.

Ostashev *et al.* (2025) further argue that for a sensor array with the diameter D, r can be approximated by D. In the experiment, $D = 0.95$ m and $\sigma_\theta = 1.75°$. Then, from Eq. (26), one has $r_{coh} = 0.66$ m for $f = 3600$ Hz. For the frequencies below 3600 Hz, the coherence radius is larger than 0.66 m and can be readily calculated with Eq. (26). Therefore, the microphone array, especially for the lower frequencies considered in this article, mostly lay withing the coherence radius, which means that random refractions affecting the wave tilt on all microphones should play a major role even after applying the correction algorithm. The results corroborate this observation.

Sec. III describes experiments and simulations that are used to quantify the effects of the proposed adjustments on two common BF techniques.

III. THEORETICAL PERFORMANCE AND PHYSICAL EXPERIMENT

The experiment was conducted at the North Hartland Dam in Hartland, VT, on August 23, 2024. This site was selected because it facilitated 1) a long propagation distance (95 m horizontally), which produced sufficiently large turbulent effects, and 2) an elevated source (35 m vertically), which raised the first Fresnel zone completely above the ground. Figure 5 depicts the location and geometry of the setup.

The acoustic source consisted of a BMS dual-diaphragm midrange compression driver (model 4599D, BMS Speakers GmbH, Hanover, Lower Saxony, Germany) mounted on the tower at an elevation of approximately 35 m above ground level. The emitted signal was intended to comprise simultaneous continuous pure tones at 225, 450, 900, 1800, and 3600 Hz. Because of overdriving of the compression driver, additional harmonic components were also present in the radiated spectrum. The signal was played continuously throughout each measurement period.

Acoustic measurements were acquired using a Nor848B Acoustic Camera (Norsonic AS, part of the RION Group, Tranby City, Buskerud County, Norway), shown in Fig. 6. The array consists of 384 InvenSense INMP521 microphones (InvenSense, Inc., San Jose, California, USA) with a sampling rate of 44.1 kHz, an

05 August 2026 16:48:48

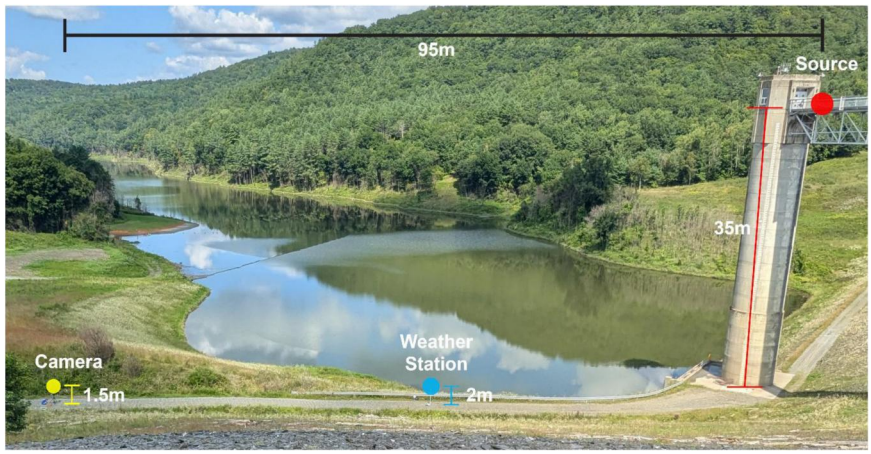


FIG. 5. Experiment geometry. Camera (yellow) at a height of 1.5 m, weather station (blue) at a height of 2 m, and sound source (red) at a height of 35 m with the horizontal offset range of 95 m from the camera.

aperture of 92 cm, and has a specified low-frequency limit of 220 Hz. The camera was positioned approximately 95 m from the source at a height of 1.5 m above ground level and oriented directly toward the tower-mounted source. The system comprises three Hextiles that may be processed with any combination of microphones.

After this experiment, validation measurements were conducted in an anechoic chamber with the source and camera separated by approximately 8 m to investigate some data irregularities. When all three Hextiles were combined into a single BF aperture, an angular wander of 1.25° was observed. In contrast, when individual Hextiles were processed independently, the measured wander ranged from 0.02° to 0.09°. These results indicate that combining the three Hextiles can introduce artificial beam wander unrelated to atmospheric turbulence. Portions of the present dataset were acquired and analyzed using the combined three-tile configuration, and this potential instrumentation-induced variability should be considered when interpreting the reported angular fluctuations without applying the proposed techniques, which filters out fluctuations in the signal because of both turbulent and instrumental noise.

A weather station was positioned approximately halfway between the source and receiver at a measurement height of 2 m above ground level. This station utilized a Vaisala WXT536 (Vaisala Oyj, Vantaa, Uusimaa Region, Finland). The station recorded air temperature, wind speed, wind direction, and relative humidity. Wind speed and direction were sampled at 20 Hz. Table II provides a brief overview of the weather conditions of the four different runs.

Measurements were conducted throughout the day to capture LoB variability under different atmospheric conditions. Four measurement sessions were completed, each lasting 20 min with 5 min of background noise measurements before and after. Additional measurements were planned; however, equipment overheating (a recording laptop) limited the total number of sessions. These corrupted data were not used in the article. During each session, the acoustic source operated



FIG. 6. Nor848b acoustic camera, three Hextile set-up.

05 August 2026 16:48:48

https://doi.org/10.1121/10.0044369

TABLE II. Runs through the day and the associated weather conditions.

	Start time (local)	Temperature (°C)	Humidity (RH[a] %)	Wind speed (m/s)
Run 1	10:14	15.4	89.2	0.7
Run 2	11:30	17.8	81.2	0.8
Run 3	14:55	21.5	61.7	1.2
Run 4	16:28	22.2	57.7	1.3

[a]Relative humidity (RH).

continuously while the acoustic camera recorded data. The Fourier spectra of a 1 s time series recorded on three microphones on panel 1 are shown in Fig. 7.

The five harmonics with the largest magnitude were analyzed, namely 225, 450, 675, 1800, and 3600 Hz. The estimated actual LoB direction to the source was $\theta_{LoB} = 90°$ and $\varphi_{LoB} = 0°$. Note that the magnitude of the Fourier transforms on three closely located microphones (less than 0.5 m apart) vary substantially, especially at the higher frequencies, which violates the analytical scenario of a single plane wave in the absence of turbulence.

Figures 8(a) and 8(b) simulate LoB estimates using DaS and MVDR BF, respectively, for the experiment setup but without turbulence. In this case, the phase distribution on the microphone array is given by Eq. (5) (the last equation); the weights are calculated for DaS and MVDR by Eqs. (8) and (9), respectively; the $\boldsymbol{R}_{xx}$ and $\boldsymbol{R}_{sx}$ matrices are constructed using Eqs. (10) and (11); the signal had a unit power; and the noise power was set to 0.1. The color represents beam power calculated by Eq. (16). For this case, a single plane wave was simulated to be incident from the direction $\theta_{LoB} = 90°$ and $\varphi_{LoB} = 0°$ to match the experiment. The angular grid resolution for both angles was 0.25°. Figures 8(c) and 8(d) show the experimental LoB estimates. For this case, empirical signals of 1 s duration were used to form the beam, and the empirically estimated matrices $\widehat{\boldsymbol{R}}_{xx}$ and $\widehat{\boldsymbol{R}}_{sx}$ to calculate the MVDR weights. As seen in Fig. 8, the actual LoB estimates are significantly worse than their theoretical counterparts: the beam power localization is distorted, the centers are misplaced, and there are much more pronounced sidelobes, which are sometimes even larger in magnitude than the mainlobe. In addition, the magnitude of the beam power is substantially different between DaS and MVDR.

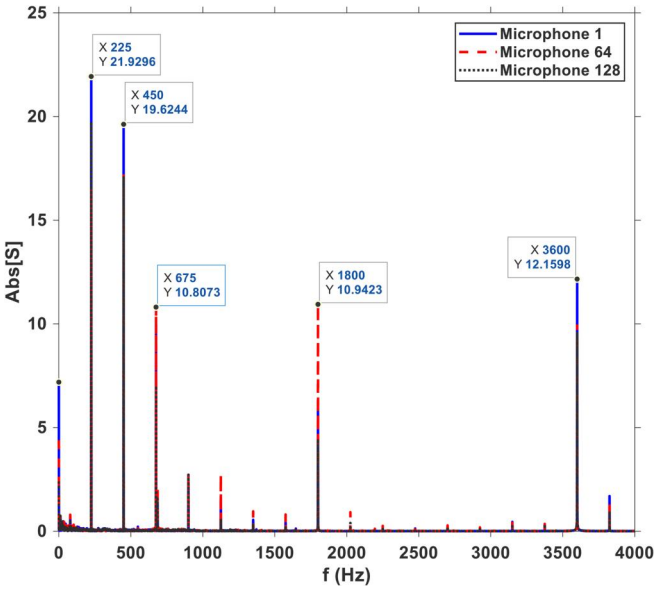


FIG. 7. Fourier spectra of signals on three microphones located within panel 1. The ordinate axis shows the absolute values of the spectra, Abs[S].

To quantify the effects of the proposed turbulence suppression method, four metrics are introduced in Table III and illustrated in Fig. 9.

The Location metric characterizes the accuracy of a LoB estimate as defined by the two angles $(\theta_{LoB}, \varphi_{LoB})$ for the source direction. Contrast quantifies the prominence of the LoB peak as the ratio of the peak power to the modal background power in decibels [see Fig. 9(a)]. The Contrast metric is similar to the Sharpness metric that is widely used in adaptive optics (Tyson and Frazier, 2022). Contrast is also practically important because power localizations with high Contrast provide a clear indication of the source direction. Width characterizes the size of a LoB peak in the (θ, φ) plane as the mean distance (in degrees) from the peak to the 3 dB down points (half peak power) in eight directions. For example, a cross section in one direction is shown in Fig. 9(b) along with the 0.5 threshold. Finally, Shape Factor is similar to eccentricity; it characterizes the shape of a LoB peak. The eight radii are determined at the 0.5 threshold as shown in Fig. 9(c), and the Shape Factor metric F is defined as the residual between 1 and the ratio of the minimum radius to the maximum radius. Ideally, the peak is a circle where $R_{min} = R_{max}$ and thus $F = 0$. At the other extreme, the peak is a line where $R_{min} = 0$ and thus $F = 1$. For any other power localization shapes, F will be in the range $[0, 1]$.

Data were processed by sequentially analyzing 1 s recorded time series during 10 min resulting in 600 frames. At each frame, three BF techniques were applied: DaS, MVDR (short-term), and MVDR (long-term). For MVDR (short-term) BF, the $\boldsymbol{R}_{xx}$ matrices are calculated for each individual frame, and for MVDR (long-term) BF, the $\boldsymbol{R}_{xx}$ matrix is the mean matrix of the 600 individual frame matrices. Figure 10 shows the 10 min time series and probability density functions (kernel estimate) of the LoB direction angles $(\theta_{LoB}, \phi_{LoB})$ obtained with DaS BF for $f = 3600$ Hz. The mean values for the angles [given in Fig. 10(a)] are close to the actual LoB to the source, with approximately 1.75° of SD for both angles. This SD is consistent with the experimental results reported in Wilson *et al.* (1999) and the theoretical predictions in Ostashev *et al.* (2025). In a homogeneous atmosphere without turbulence and noise, the SDs would ideally be zero.

Analogous calculations were conducted for five frequencies and two other BF techniques: short-term and long-term MVDR. The results for $(\theta_{\mathrm{LoB}}, \varphi_{\mathrm{LoB}})$ are presented in Fig. 11. The left column shows the conventional BF results, and the right column show the adaptive BF results using Eqs. (17)–(22). Comparing Figs. 11(a) and 11(b) reveals

05 August 2026 16:48:48

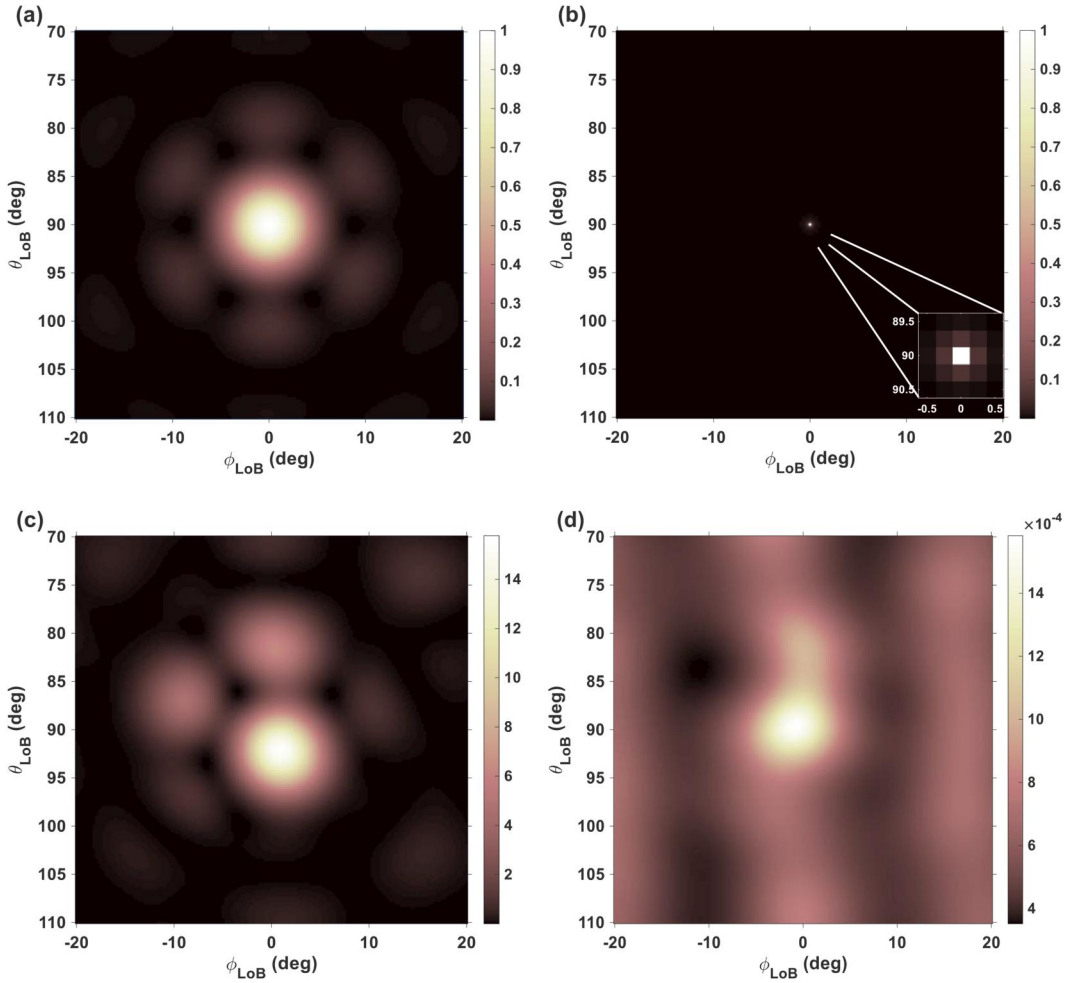


FIG. 8. Theoretical and experimental LoB estimates for single frequency BF, $f = 3600$ Hz. The color represents beam power. (a) Theoretical DaS, (b) theoretical MVDR. The inset in the lower right corner shows a zoomed-in image around the beam power peak. (c) Experimental DaS, (d) experimental short-term MVDR. deg, degrees.

that the performance of all the algorithms is rather poor for low frequencies (225, 450, and 675 Hz), which can be explained by the small size of the camera compared to the wavelength. Although DaS and short-term MVDR produce nearly identical results, their mean values lie far from the actual direction, and the SD reaches almost 10° at $f = 450$ Hz [Fig. 11(a)].

The long-term MVDR has more accurate estimates of the mean θ_{LoB} but the highest uncertainty, $\sigma_{\theta_{LoB}} \cong 15°$ at $f = 225$ Hz. At higher frequencies (1800 and 3600 Hz), the BF techniques converge to approximately the same performance, $\mu_{\theta_{LoB}} = 91.9°$ and $\sigma_{\theta_{LoB}} \cong 1.9°$. Similar features are observed for φ_{LoB} [Fig. 10(c)]. Note that the convergent value of $\mu_{\theta_{\mathrm{LoB}}} = 91.9°$ is biased relative to the actual value $\theta_{\mathrm{LoB}} = 90°$. This bias can be attributed to large phase distortions on one of the three panels in the acoustic camera, which were revealed during signal analysis (see Fig. 4). Using the adaptive algorithms made the results of DaS and short-term MVDR identical but did not improve them for lower frequencies, where the mean values for both angles remained similar (or even degraded) and the SDs even increased. At higher frequencies, all three algorithms, again, converged to the same values, $\theta_{\mathrm{LoB}} = 90°$ and $\varphi_{\mathrm{LoB}} = 0°$, which does correspond to the actual values. However, the performance of the long-term MVDR improved remarkably. Of the three BF approaches, long-term MVDR provided the

TABLE III. Metrics for quantitative analysis of BF performance.

Metric type	Description	Definition	Units
1. Location	LoB	θ_{LoB}, φ_{LoB}	Degrees
2. Contrast	The ratio of peak beam power P_{max} to background power P_0	$C = 10\log_{10}(P_{max}/P_0)$	dB
3. Width	Half-width of the beam power peak	R_{mean} over 8 directions in the (θ, φ) plane	Degrees
4. Shape Factor	Beam power peak shape	$F = 1 - R_{min}/R_{max}$	Unitless

05 August 2026 16:48:48

https://doi.org/10.1121/10.0044369

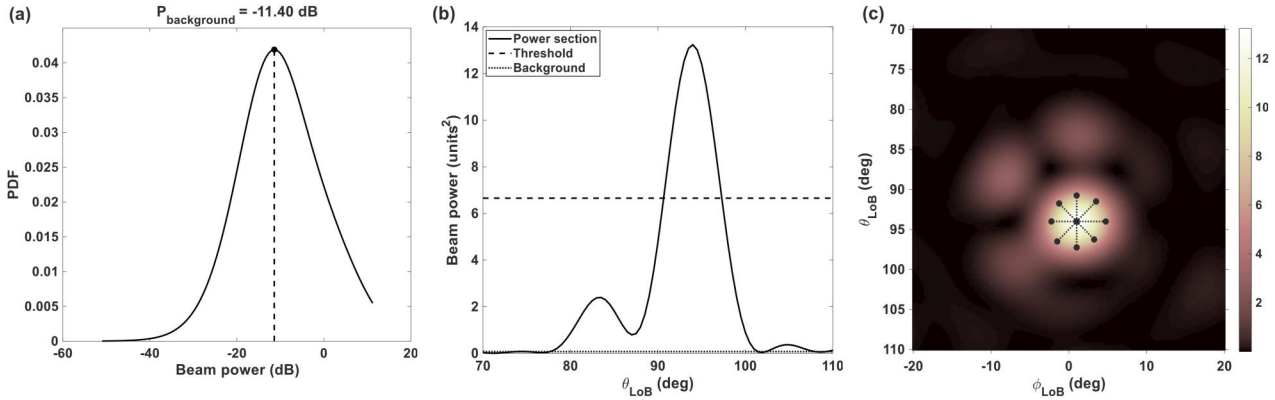


FIG. 9. Metrics to compare the quality of BF estimates. (a) Estimate of the background power P_0 as the probability density function (PDF) maximum for the Contrast metric, (b) threshold at the 0.5 level in a single direction, (c) determination of eight radii at the 0.5 level for the Width and Shape metrics. deg, degrees.

best LoB estimates in terms of the Location metric, and its SD dropped by as much as 12 times for the lower frequencies and by as much as 3 times for the higher frequencies, where the SD was approximately 0.4°.

A plausible explanation for why DaS and short-term MVDR BF have not improved significantly is that the proposed algorithm operates only with the signals observed on the acoustic camera aperture. The algorithm filters out, therefore, only distortions that are smaller than the array aperture, but the angles of arrival might still be affected by random refraction because of the random part of the wavefront tilt rather than small-scale distortions. For $f = 3600$ Hz, the estimated coherence radius is $r_{coh} = 0.66$ m, which is on the order of D, and the coherence radius is larger for $f < 3600$ Hz. If turbulence causes plane wave refraction on the microphone array aperture, which leads to an incorrect estimate of the direction of arrival, it will remain a perfectly legitimate plane wave but will be perceived to be propagating from the wrong direction. The proposed algorithm cannot resolve this issue. To more effectively mitigate refraction, one should either use a larger aperture array or several widely separated arrays. In contrast to the short-term MVDR and DaS techniques, which only use 1 s of data for each frame, the long-term MVDR uses all 10 min of observation (600 samples) to average out the effects of random signal refractions, which converges to the actual LoB signal direction, on average.

However, the proposed algorithm did improve the other three metrics. The left and right columns in Fig. 12 depict the metrics using standard and adaptive algorithms, respectively.

The mean Contrast of the beam power increases as the frequency increases, and the highest mean contrast is observed for DaS and long-term MVDR; although they also have the highest SD (about 4 dB), as well [Fig. 12(a)]. For short-term MVDR, the proposed algorithm increases the mean Contrast by about 100 dB but has mixed results for the SD [i.e., an increase to 4 dB at low frequencies and a decrease to 1 dB at high frequencies; Fig. 12(b)]. The mean Contrast for DaS and long-term MVDR slightly increases as well, and the SD for DaS drops below 1 dB, whereas for long-term MVDR, it increases from 1 dB for low

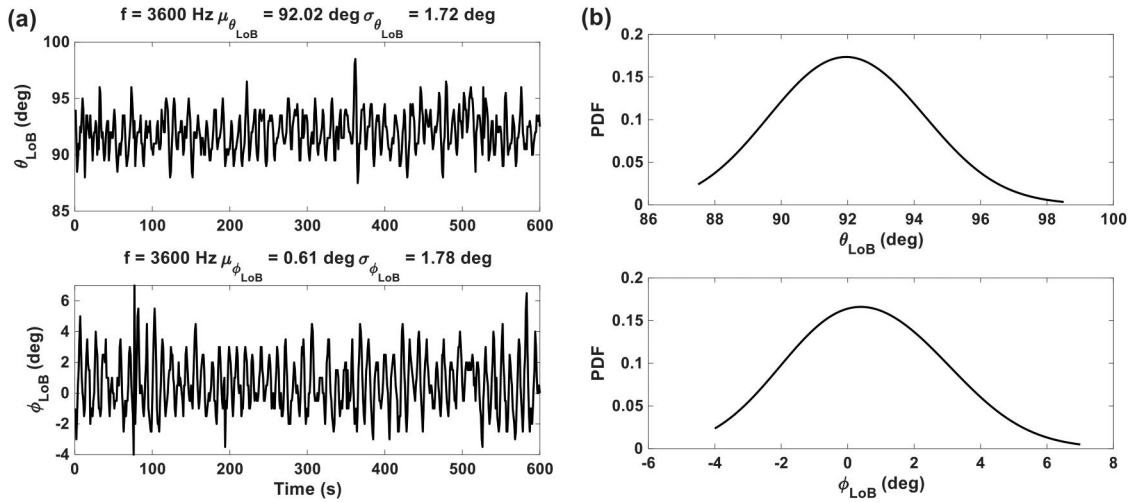


FIG. 10. Estimation of LoB direction using DaS BF for $f = 3600$ Hz. (a) Time series, (b) kernel density estimates for the probability distributions of the angles. deg, degrees.

05 August 2026 16:48:48

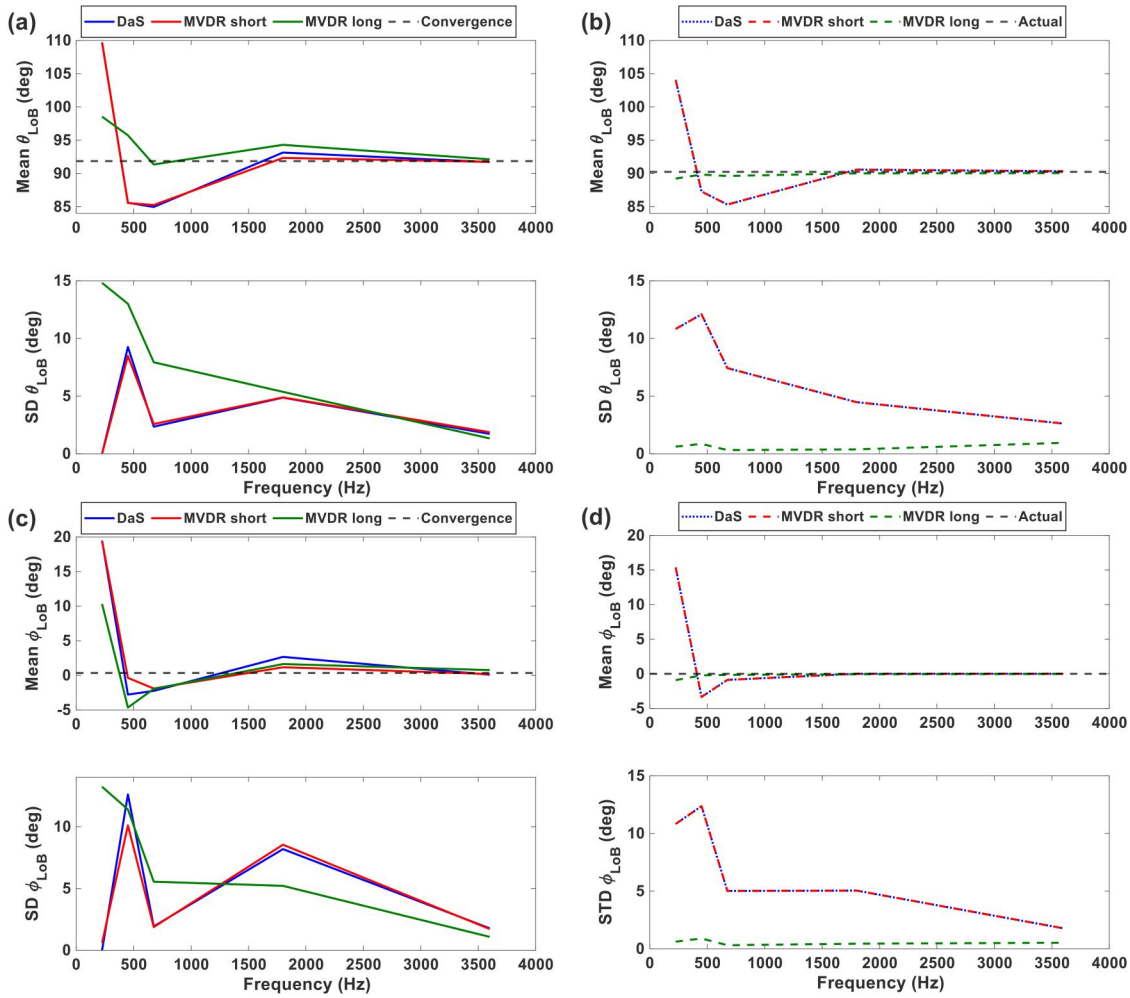


FIG. 11. Performance of the beamformers for estimates of the LoB direction by standard (left column) and proposed turbulence adaptive (right column) algorithms. (a) and (b) Mean (top plot) and SD (bottom plot) of θ_{LoB}, (c) and (d) mean (top plot) and SD (bottom plot) of φ_{LoB}. deg, degrees.

frequencies (225 Hz) to above 4 dB for high frequencies (3600 Hz). The mean Width of DaS does not change appreciably, although its SD decreases [Figs. 12(c) and 12(d)]. In contrast, the mean Widths for the short-term and long-term MVDR decrease noticeably, from about 5° to 1°, and their SDs decreased to a fraction of 1°, meaning that the beam power became repeatably very well localized. DaS had the best Shape performance (having a more circular and symmetric beam power localization) with low SD [Fig. 12(e)]. The proposed algorithm improved it further and reduced its SD [Fig. 12(f)]. However, the short-term MVDR was the most impacted; the proposed algorithm made the beam localization very sharp, basically reducing it to a single pixel, as shown in the Fig. 8(b) inset plot. For such a limiting case, the Shape metric reduces to 0.29 (because of purely geometric reasons on the square grid), with zero SD, as observed in Fig. 12(f). In contrast, the Shape performance of the long-term MVDR deteriorated: the mean Shape became higher (less circular on average), and its SD became the highest of all three BF techniques.

Table IV summarizes the results of the BF performance with turbulence suppression, averaged across all frequencies, with respect to the tested metrics. The figure in the parenthesis next to the mean values indicate the rank: 1, the best of three considered BF techniques; 2, second best; and 3, the worst.

In summary, from Figs. 11 and 12, and Table IV, the proposed algorithm for adaptive suppression of turbulence effects made long-term MVDR the best overall (best for accuracy and stability of the LoB direction, second best in Contrast, a tie for best in Width, but somewhat worse in Shape). Short-term MVDR is second best overall with the highest Contrast and the smallest localization area.

IV. DISCUSSION

The performance of conventional BF algorithms, which assume a homogeneous propagation medium, degrades in a turbulent atmosphere. This degradation is because of random distortions of both the amplitude and phase of the incident signal. To mitigate these effects, two principal ways seem feasible. The first approach is to modify the BF

05 August 2026 16:48:48

https://doi.org/10.1121/10.0044369

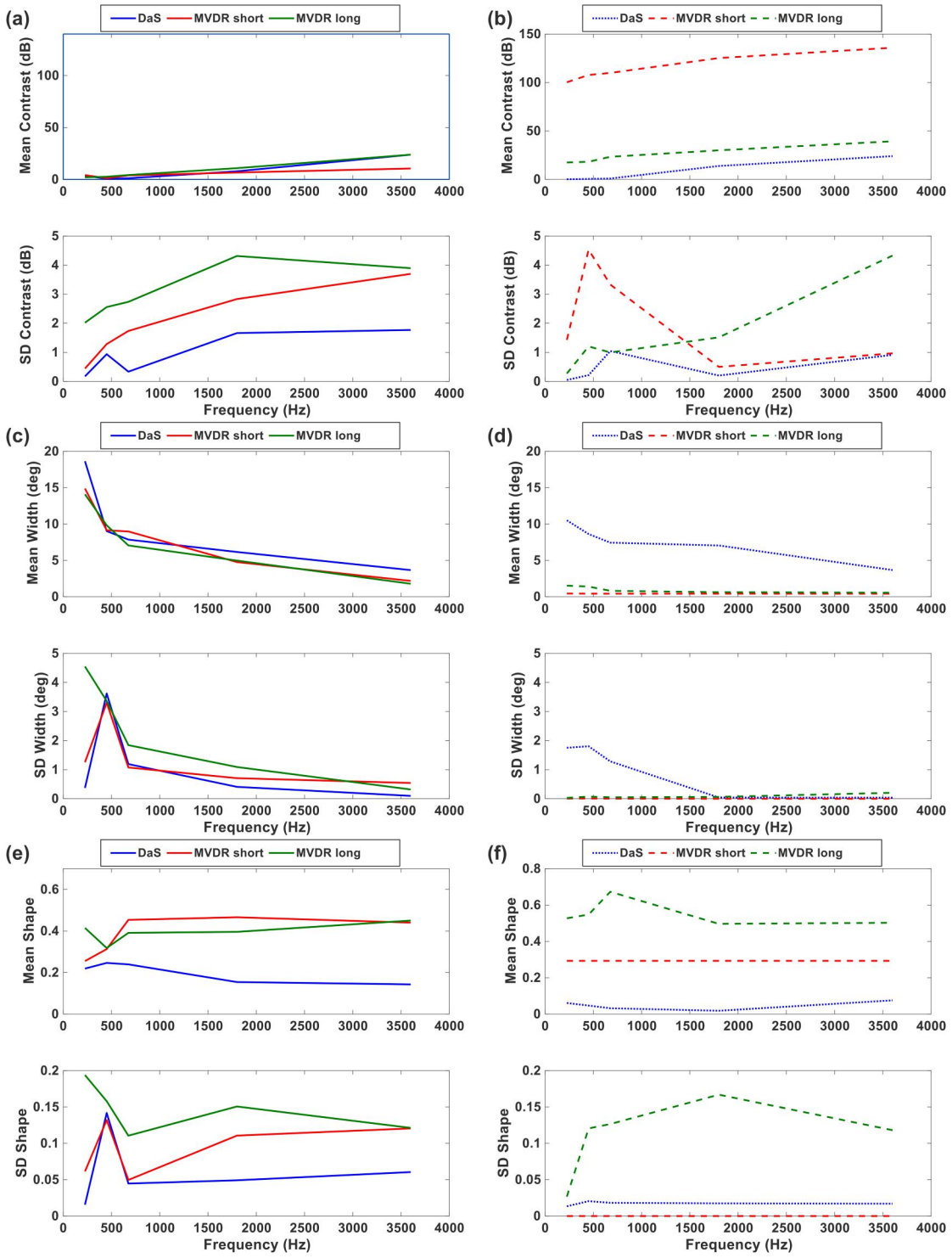


FIG. 12. Performance of BF techniques using standard (left column) and proposed turbulence adaptive (right column) algorithms for Contrast, Width, and Shape Factor metrics. (a) and (b) Mean (top plot) and SD (bottom plot) of Contrast, (c) and (d) mean (top plot) and SD (bottom plot) of Width, (e) and (f) mean (top plot) and SD (bottom plot) of Shape Factor.

mathematical and statistical framework to account for medium inhomogeneities and randomness, and the second approach is to preprocess the data so they fit the modeling assumptions of the classical BF algorithms. Because the instantaneous state of the turbulence is unknown, the first approach is only realizable in a statistical sense through ensemble averaging. This choice leads to the assumption of a turbulence spatial spectrum (e.g., von Karman or Kolmogorov) and the utilization of mutual coherence functions (see, for example, Ostashev *et al.*, 1998; Collier, 2005; Collier *et al.*, 2005; Ostashev and Wilson, 2026). Such a formulation eventually results in a mathematical framework

05 August 2026 16:48:48

TABLE IV. Performance rating of three tested beamformers with turbulence suppression.

		DaS	Short-term MVDR	Long-term MVDR
θ_{LoB}, deg	Mean	91.53 (2)[a]	91.53 (2)	89.76 (1)[b]
	SD	7.49 (2)	7.49 (2)	0.63 (1)
φ_{LoB}, deg	Mean	2.25 (2)	2.25 (2)	−0.26 (1)
	SD	7.01 (2)	7.01 (2)	0.56 (1)
Contrast, dB	Mean	7.92 (3)[c]	115.80 (1)	25.70 (2)
	SD	0.49 (1)	2.15 (3)	1.66 (2)
Width, deg	Mean	7.46 (3)	0.43 (1)	0.99 (2)
	SD	0.98 (3)	0.0042 (1)	0.084 (2)
Shape Factor	Mean	0.047 (2)	0.29 (1, single pixel)	0.55 (3)
	SD	0.017 (2)	0.00 (1)	0.11 (3)

[a](2) Indicates second best.
[b](1) Indicates the best.
[c](3) Indicates the worst.

that is substantially different from the classical BF framework (e.g., Bayesian estimation or maximum likelihood) and only improves source localization in the ensemble (averaged) sense, which requires a relatively long measurement time. Instantaneous errors in the source locations could be significant. This article takes the second approach, which preserves the classical BF framework by suppressing the instantaneous fluctuations in the data. Instead of modifying the mathematical framework to include the turbulence effects in the ensemble sense, it filters the measured signals to remove the turbulent effects. After such filtration, which applies to instantaneous measurements, any BF algorithm can be used.

The proposed algorithm spatially filters the data phases using Zernike polynomials, and modifies the amplitudes leveraging knowledge about the analytical covariance matrix. Both modifications assume only one incident plane wave, e.g., a single distant source. Generalizing this method to multiple sources and non-plane wave signals is possible but non-trivial. The main difficulty is that the spatial distribution of the amplitude and phase is unknown for multiple sources. For an incident plane wave from any direction, the phase on a planar microphone array can be expressed using only three Zernike polynomials. However, for multiple sources, this simple approach is insufficient, and more research is required to determine how many terms are sufficient and whether this number depends on the incident direction. Alternatively, the proposed algorithm for phase adjustment could be applied for all possible incident directions one at a time, and then several best directions could be identified, corresponding to multiple sources. However, the signal amplitude would not be simply attributed to any specific direction and would remain unfiltered. The performance of such a method for multiple sources requires further investigation.

V. CONCLUSION

Acoustic turbulence introduces signal amplitude and phase fluctuations that cause a shifted, blurred, enlarged, and irregular beam energy pattern, which degrades the performance of BF techniques. This paper developed an approach to mitigate these turbulence effects by preprocessing the sensor data while assuming a single, stationary, and monochromatic source; a generalization to broadband, non-plane wave, or multiple sources is deferred to future work. The measured phase was adjusted to eliminate small-scale variations using the Zernike polynomials, and the measured amplitude was adjusted to match the analytical covariance matrix derived with the plane wave approximation without turbulence. The proposed technique was evaluated using three common BF algorithms on acoustic camera data. The results indicate that the elimination of small-scale (compared to the array aperture), non-plane wave distortions (because of turbulence, clutter, and instrumental noise) mostly improved the Shape Factor, Contrast, and Width of the beam patterns, and less so the Location accuracy. The main limitation is that large-scale turbulence variations cause fluctuations in the apparent LoB while remaining planar on the array aperture. In other words, random refractions play a more significant role for the LoB estimation accuracy. Mitigating these large-scale effects with the proposed approach would require a larger array aperture or multiple separated arrays. After applying the proposed technique, the long-term (10 min) MVDR BF technique had the best overall performance and was also the most improved, which was followed by short-term MVDR and DaS. Therefore, when the situation allows, a longer data collection should be used to better estimate the adjusted covariance matrix.

ACKNOWLEDGMENTS

This research was funded by the U.S. Army Engineer Research and Development Center basic research program. Permission to publish was granted by Director, Cold Regions Research and Engineering Laboratory. We also want to thank the U.S. Army Corps of Engineers, New England District, for letting us use the North Hartland Dam for the experiment.

AUTHOR DECLARATIONS

Conflict of Interest

The authors have no conflicts to disclose.

DATA AVAILABILITY

The data that support the findings of this study are available from the corresponding author upon reasonable request.

Andrews, L., and Phillips, R. (**2005**). *Laser Beam Propagation through Random Media* (2nd Edition, SPIE Press, Bellingham, WA).

Bell, K. L., Ephraim, Y., and Van Trees, H. L. (**2000**). "A Bayesian approach to robust adaptive beamforming," IEEE Trans. Signal Process. **48**(2), 386–398.

Bell, K. L., and Van Trees, H. L. (**1998**). "Adaptive beamforming for spatially spread sources," in *Ninth IEEE Signal Processing Workshop on Statistical Signal and Array Processing (Cat. No. 98TH8381)*, IEEE, September 14–16, Portland, OR, pp. 1–4.

05 August 2026 16:48:48

Brown, E. H., and Hall, F. F., Jr. (**1978**). "Advances in atmospheric acoustics," Rev. Geophys. **16**, 47–110, https://doi.org/10.1029/RG016i001p00047.
Collier, S. L. (**2005**). "Fisher information for a complex Gaussian random variable: Beamforming applications for wave propagation in a random medium," IEEE Trans. Signal Process. **53**, 4236–4248.
Collier, S. L., Ostashev, V. E., and Wilson, D. K. (**2005**). "Angle-of-arrival estimation for acoustic waves propagating in atmospheric turbulence," in *Proceedings of Forum Acusticum Budapest 2005: 4th European Congress on Acustics*, European Acoustics Association Budapest, Hungary, August 29–September 2. Paper 732–0.
Dougherty, R. P. (**2002**). "Beamforming in acoustic testing," in *Aeroacoustic Measurements*, edited by C. S. Allen, W. K. Blake, R. P. Dougherty, D. Lynch, P. T. Soderman, J. R. Underbrink, and T. J. Mueller (Springer, Berlin), pp. 62–97.
Hou, H., Ning, F., Jia, D., Li, W., and Wei, J. (**2024**). "Hybrid deconvolution method based on mode composition beamforming for separating sound sources with different motion modes," J. Sound Vib. **593**, 118654.
Intema, H., van der Tol, S., Cotton, W., Cohen, A., van Bemmel, I., and Röttgering, H. (**2009**). "Ionospheric calibration of low frequency radio interferometric observations using the peeling scheme," Astron. Astrophys. **501**, 1185–1205.
Itzhak, G., and Cohen, I. (**2024**). "Robust beamforming for multispeaker audio conferencing under DOA uncertainty," IEEE Trans. Audio. Speech Lang. Process. **33**, 139–151.
Licitra, G., Artuso, F., Bernardini, M., Moro, A., Fidecaro, F., and Fredianelli, L. (**2023**). "Acoustic beamforming algorithms and their applications in environmental noise," Curr. Pollut. Rep. **9**, 486–509.
Lukin, V. P. (**1996**). *Atmospheric Adaptive Optics* (SPIE Press, Bellingham, WA).
Meyer, A. C., Doran, A. K., Wilson, D. K., Kamrath, M. J., Romond, R. A., and Ostashev, V. E. (**2025**). "Localizing acoustic sources in an urban environment with deep signal fading," J. Acoust. Soc. Am. **158**, 433–446.
Moran, M. L., Greenfield, R. J., and Wilson, D. K. (**2007**). "Acoustic array tracking performance under moderately complex environmental conditions," Appl. Acoust. **68**, 1241–1262.
OEIS Foundation Inc. (**2026**). "Entry A176988," in The Online Encyclopedia of Integer Sequences, https://oeis.org/A176988.
Ostashev, V., Brähler, B., Mellert, V., and Goedecke, G. (**1998**). "Coherence functions of plane and spherical waves in a turbulent medium with the von Karman spectrum of medium inhomogeneities," J. Acoust. Soc. Am. **104**, 727–737.
Ostashev, V. E., Breton, D. J., and Wilson, D. K. (**2024**). "Interference of the direct and ground-reflected waves in the atmosphere with volumetric scattering," J. Acoust. Soc. Am. **156**, 107–118.
Ostashev, V. E., Muhlestein, M. B., Wilson, D. K., Vecherin, S. N., Eggleston, M. L., Kamrath, M. J., and Gee, K. L. (**2025**). "Angle-of-arrival fluctuations in a turbulent atmosphere," J. Acoust. Soc. Am. **158**, 2714–2722.
Ostashev, V. E., and Wilson, D. K. (**2026**). *Acoustics in Moving Inhomogeneous Media*, 3rd ed. (CRC Press, Boca Raton, FL).
Ostashev, V. E., Wilson, D. K., and Colosi, J. A. (**2021**). "Valerian Tatarskii and acoustic wave propagation in random media," Acoust. Today **17**, 38–47.
Phillips, R., Andrews, L., Stryjewski, J., Griffis, B., Borbath, M., Galus, D., Burdge, G., Green, K., Kim, C., and Stack, D. (**2006**). "Beam wander experiments: Terrestrial path," Proc. SPIE **6303**, 62–70.
Prime, Z., and Doolan, C. (**2013**). "A comparison of popular beamforming arrays," in *Proceedings of ACOUSTICS 2013—Victor Harbor*, Australian Acoustical Society, November 17–20, Victor Harbor, Australia, Vol. 1, 5.
Rytov, S., Kravtsov, Y. A., and Tatarskii, V. (**1989**). *Principles of Statistical Radiophysics 4: Wave Propagation Through Random Media* (Springer, Berlin).
Song, X., Wang, J., and Wang, B. (**2009**). "Robust adaptive beamforming algorithm under directional uncertainty," in *Proceedings of the 2009 Chinese Control and Decision Conference* (IEEE), June 17–19, Guilin, China, pp. 2842–2845.
Stoica, P., Wang, Z., and Li, J. (**2002**). "Robust capon beamforming," in *Proceedings of the Conference Record of the Thirty-Sixth Asilomar Conference on Signals, Systems and Computers, 2002* (IEEE), November 3–6, Pacific Grove, CA, pp. 876–880.
Tatarskii, V. I. (**1971**). "The Effects of the Turbulent Atmosphere on Wave Propagation", Technical Report No. 197205 (National Science Foundation, Washington, DC).
Tyson, R. K., and Frazier, B. W. (**2022**). *Principles of Adaptive Optics* (CRC Press, Boca Raton, FL).
Wilson, D. K., Tate, C. R., Swanson, D. C., and Reichard, K. M. (**1999**). "Acoustic scintillations and angle-of-arrival fluctuations observed outdoors with a large planar vertical microphone array," J. Acoust. Soc. Am. **106**, L24–L29.
Yang, J., Yang, Y., and Liao, B. (**2025**). "Robust Bayesian acoustic DOA estimation with passive synthetic aperture arrays," IEEE Trans. Aerosp. Electron. Syst. **61**, 4178–4191.
Zhang, X., Chen, Z., Yu, X., Lin, B., Ma, Z., Zhu, J., Wang, P., and Li, J. (**2025**). "A novel two-stage DOA estimation of sound sources based on hierarchical sparse Bayesian inference," Appl. Acoust. **231**, 110514.
Zhao, X., Luo, X., Huang, G., Chen, J., and Benesty, J. (**2024**). "Differential beamforming with null constraints for spherical microphone arrays," in *Proceedings of ICASSP 2024–2024 IEEE International Conference on Acoustics, Speech and Signal Processing (ICASSP)* (IEEE), April 14–19, Seoul, South Korea, pp. 776–780.

05 August 2026 16:48:48